0D/1D CuO-Cu2O/ZnO p-n heterojunction with high photocatalytic activity for the degradation of dyes and Naproxen

Mouna Ibn Mahrsi, Bilel Chouchene, Thomas Gries, Vincent Carré, Ghouti Medjahdi, Fadila Ayari, Lavinia Balan, Raphaël Schneider

0D/1D $CuO-Cu_2O/ZnO$ p-n heterojunction with high photocatalytic activity for the degradation of dyes and Naproxen

Mouna Ibn Mahrsi,[a,b] Bilel Chouchene,[a] Thomas Gries,[c] Vincent Carré,[d] Ghouti Medjahdi,[c] Fadila Ayari,[b] Lavinia Balan,[e] Raphaël Schneider [a*]

[a] Université de Lorraine, CNRS, LRGP, F-54000 Nancy, France

[b] Carthage University, Faculty of Sciences of Bizerte, LR 05/ES09 Laboratory of Applications of Chemistry to Resources and Natural Substances and to the Environment (LACReSNE), Zarzouna 7021, Tunisia

[c] Université de Lorraine, CNRS, IJL, F-54000 Nancy, France

[d] Université de Lorraine, LCP-A2MC, F-57000 Metz, France

[e] CEMHTI-UPR 3079 CNRS, Site Haute Température, 1D avenue de la Recherche Scientifique, 45071 Orléans, France

[*] Corresponding author. E-mail address: raphael.schneider@univ-lorraine.fr

Abstract. The development of highly active photocatalysts with broad spectrum response is of paramount importance for photocatalytic applications. Herein, heterostructured $CuO-Cu_2O/ZnO$ photocatalysts were prepared in a single step and under mild conditions using a photodeposition process which allows to deposit $CuO-Cu_2O$ particles with an average size of ca. 2.4 nm on the surface of ZnO nanorods. The p-n heterojunction built between $CuO-Cu_2O$ and ZnO allows to increase both the visible light response of the photocatalyst and the charge separation. The $CuO-Cu_2O(10\%)/ZnO$ catalyst exhibits the highest activity for the degradation of dyes (Rhodamine B and Remazol Brilliant Blue R) and of Naproxen under simulated solar light irradiation. Based on scavenging experiments, holes, superoxide radicals $O_2^{\bullet-}$ and singlet oxygen $^1O_2$ are the dominant species involved in the photocatalytic degradation and a mechanism is proposed. Due to its high stability and photocatalytic performance in various water matrices, the $CuO-Cu_2O(10\%)/ZnO$ nanohybrid is of high potential for the large scale remediation of organic pollutants in wastewater.

Keywords: heterostructured photocatalyst; CuO-Cu_2O/ZnO; photocatalytic degradation; Naproxen

1. Introduction

In the past few decades, environmental pollution by persistent organic compounds has generated serious toxicity problems both for living beings but also for ecological systems. Photocatalysis is a green advanced oxidation process (AOP) for environmental remediation as this technique requires only a catalyst and light to decompose pollutants [1]. Upon irradiation of the semiconductor photocatalyst, electrons are promoted to the conduction band while holes remain in the valence band. The electron/hole charge carriers take part in redox reactions with oxygen and water allowing the production of oxidative species such as superoxide $O_2^{\bullet-}$ and hydroxyl $^{\bullet}OH$ radicals or hydrogen peroxide H_2O_2 that decompose the pollutants. ZnO is a well-known n-type semiconductor exhibiting a high photocatalytic activity, low cost and weak toxicity and has therefore found many environmental [2-6] or energy applications like hydrogen production via water splitting [7,8] or CO_2 reduction [8]. However, ZnO exhibits drawbacks like the fast recombination of electron/hole pairs and the weak absorption of visible photons (energy bandgap of 3.3 eV) which restrict its photocatalytic activity [2-6]. Among the strategies developed to overcome these disadvantages are the doping of ZnO with metals or non-metals [5,10] or the construction of heterojunctions with smaller bandgap semiconductors that allows mutual transfer of charge carriers [11,12]. CuO and Cu_2O are p-type low bandgap semiconductors (ca. 1.85 and 2.0-2.2 eV for bulk CuO and Cu_2O, respectively) [13] that can be coupled to ZnO to form p-n heterostructures that allow to decrease the electron/hole recombination and increase the visible light response. In recent years, numerous syntheses of CuO or Cu_2O/ZnO heterostructures have been developed among which the co-precipitation [14,15], the wet chemical [16], the sol-gel followed by calcination [17,18], the ball milling [19], the solution combustion [20], the solid state reaction [21], the oxidation of Cu(0)-coated ZnO [22] or the use of metal organic frameworks as templates [23] can be cited. However, most of these methods do not allow precise control of the size and distribution of copper oxide nanoparticles associated to ZnO.

Recently, there has been a notable focus on developing three-component photocatalysts that integrate CuO, Cu_2O, and ZnO to enhance charge carrier separation and, consequently, improve photocatalytic activity. However, the expedited and straightforward synthesis of such catalysts poses a challenge, primarily due to the presence of copper in two oxidation states (+1 and +2). To the best of our knowledge, only three syntheses of photocatalysts associating CuO, Cu_2O and ZnO were reported. CuO-Cu_2O/ZnO photocatalysts can be prepared by controlled oxidation of preformed CuS/ZnO composite [24], by a microwave-assisted sol-gel process in the presence of a reductant [25] or via the combustion method using oxalyldihydrazide as fuel [26]. These multi-stage processes require high temperature heating and/or specific gas mixtures (N_2/O_2) to obtain the desired CuO-Cu_2O/ZnO catalysts.

The photodeposition has been demonstrated to be a mild and easy method to associate metal or metal oxide nanoparticles with a semiconductor as it requires only a light source [26]. The photodeposition of metallic Cu [28-30] or more rarely CuO [31-33] on the surface of ZnO is described in the literature and this process has been demonstrated to be of high potential for the preparation of heterostructured photocatalysts. Moreover, depending on the irradiation conditions and on the presence of surfactants in the reaction medium, the size and the morphology of copper oxide nanoparticles can easily be tuned from pseudo-spherical to nanoplates [31-33].

Herein, we report a single-step photodeposition process for the preparation of nanometer-sized CuO-Cu_2O particles on the surface of ZnO NRs exhibiting an average length of 150 nm and a diameter of 35 nm. The obtained CuO-Cu_2O/ZnO heterostructures were demonstrated to be highly effective photocatalysts for the photocatalytic degradation of dyes (Rhodamine B and Remazol Brilliant Blue R) and of Naproxen under simulated solar light irradiation. Our findings illustrate that the p-n heterojunction formed between CuO-Cu_2O and ZnO particles not only enhances the catalysts response to visible light but also improves the separation of photo-generated charge carriers.

2. Experimental section

2.1. Materials

$Zn(OAc)_2 \bullet 2H_2O$ (Merck, >99%), $Cu(NO_3)_2 \bullet 3H_2O$ (Merck, >99%), tert-butanol (t-BuOH, Merck, >99%), 4-hydroxy-2,2,6,6-tetramethylpiperidine-1-oxyl (TEMPOL, Merck, >98%), ethylenediaminetetraacetic acid disodium salt (EDTA, Fisher, >99%), dimethylsulfoxyde DMSO (Merck, >99.9%), sodium azide (Merck, >99%), Rhodamine B (RhB, Merck, analytical standard), Remazol Brilliant Blue R (RBBR, Merck), (S)-(+)-2-(6-Methoxy-2-naphthyl)propionic acid (Naproxen, Fisher, 99%) and absolute ethanol (VWR) were used as received.

2.2. Synthesis of ZnO NRs

ZnO NRs were prepared by a solvothermal process using $Zn(OAc)_2$ as precursor [4]. Briefly, $Zn(OAc)_2 \bullet 2H_2O$ (511 mg) was dissolved in absolute ethanol (35 mL) (Solution A) and NaOH (466 mg) in ethanol (35 mL) (Solution B). Then, solution B was dropwise added to solution A and the mixture stirred for 30 min at room temperature. The mixture was then transferred into a Teflon autoclave, sealed and heated at 160°C for 24 h. After natural cooling, the white ZnO powder obtained after centrifugation (4000 rpm for 15 min) was washed with water (4 x 20 mL), with ethanol (4 x 20 mL) and dried at 70°C for 15 h.

2.3. Synthesis of CuO-Cu_2O/ZnO heterostructured photocatalysts

The photodeposition of CuO-Cu_2O particles on the surface of ZnO NRs was conducted by irradiating a dispersion of ZnO NRs and $Cu(NO_3)_2$ with a 150 W Xe lamp. Briefly, for the preparation of the CuO-Cu_2O(10%)/ZnO nanohybrid, 150 mg of ZnO NRs and $Cu(NO_3)_2$ (53.1 mg, 2.19 mmol) were dispersed in 110 mL of a water/ethanol 10:1 (vol/vol) mixture and the pH adjusted to 9.5 using 1 M aqueous NaOH and HCl. Next, the Xe lamp was turned on and the mixture irradiated for a period of 6 h (irradiance of 30 mW/cm^2) under stirring. The CuO-Cu_2O (10%)/ZnO nanohybrid was collected by centrifugation and washed with water (2 x 50 mL). The bright green CuO-Cu_2O (10%)/ZnO nanhybrid was then dried in air at 100°C for 6 h. Nanohybrids containing 5 and 20% CuO-Cu_2O were prepared via the same synthetic protocol but using 26.5 and 106.2 mg of $Cu(NO_3)_2$ as precursor, respectively.

2.4. Characterizations

The crystallinity and phase of the photocatalysts were characterized by X-ray diffraction (XRD, Panalytical X'Pert pro MPD diffractometer with Cu Kα radiation = 0.15406 nm) and high resolution transmission electron microscopy (HR-TEM, Philips CM200 equipment operating at an acceleration voltage of 200 kV equipped with energy dispersive X-ray (EDX) spectrometer). The morphology of the photocatalysts was determined by scanning electron microscopy (SEM, JEOL JSM-6490 LV and JEOL JSM IT800 instruments) and TEM. The purity, the surface composition and the chemical state of elements were inspected by X-ray photoelectron spectroscopy (XPS) using a Gammadata Scienta SES 200-2 spectrometer. The chemical functions present in the photocatalysts were investigated using Fourier transform-infrared (FT-IR) spectroscopy (Brucker ALPHA II FT-IR spectrometer) and Raman spectroscopy (Horiba Xplora spectrometer) using a 532 nm Nd:YAG laser. The Zeta potential of the photocatalysts was measured using a Malvern Zetasizer Nano ZS equipment.

The evolution of photocatalysis reactions was monitored by UV-visible absorption spectroscopy in liquid phase (Thermo Scientific Evolution 220 spectrometer). The electronic properties of the photocatalysts were analysed by UV-visible diffuse reflectance spectroscopy (DRS, Shimadzu 2600-2700 spectrometer) and photoluminescence (PL, Horiba Fluoromax) equipped with a Xenon lamp as the excitation source. The total organic carbon (TOC) was used to determine the mineralization degree (Shimadzu TOC-V_{CSH} analyzer).

LC-UV-MS and MS2 analyses were performed using a Dionex Ultimate 3000 (Thermo Fisher Scientific, France) and a linear ion trap mass spectrometer (LTQ Velos Pro, Thermo Fisher Scientific, MA, USA). A C18 reverse-phase column (Accucore C18, 2.1 x 100 mm, 2.6 µm, Thermo Fisher Scientific, France) maintained at a constant temperature of 30°C was employed. For each analysed sample, 20 µL was injected. LC system delivered continuously 0.250 $mL.min^{-1}$ flow rate. Throughout the LC run, the column outlet flow was equally divided, one stream for UV detection at 230 and 340 nm wavelengths, and the other for MS measurement.

Initially, a mobile phase consisting of 5% acetonitrile and 95% water (buffered with 50 mM of CH_3COONH_4) was held for 5 min, followed by a linear elution gradient for 25 min reaching 80% acetonitrile.

For MS measurement, the electrospray ionization source was used working at 4.7 kV (200°C and N_2 as the nebulizer gas). Mass spectrometry scanned from 90 to 1000 m/z in positive ion

157 detection mode. For chromatographic peak confirmation, MS2 was systematically performed
158 by collision induced dissociation at 20 eV or 30 eV on $[M+H]^+$ or $[M+NH_4]^+$ ions.
159 Potentiostatic electrochemical impedance spectroscopy (EIS) was conducted from 500 kHz
160 to 10 mHz for low amplitudes of ± 10 mV at open circuit potential (OCP) under dark
161 condition using a potentiostat BioLogic SP150 in a conventional three electrode cell with a Pt
162 coil as the counter electrode, a Ag/AgCl electrode in saturated KCl as reference electrode
163 and FTO glass uniformly coated with as-prepared photocatalysts as working electrode. The
164 electrolyte was a 0.1 M Na_2SO_4 aqueous solution.
165
166 2.5. Photocatalytic activity
167
168 The performance of CuO-Cu_2O/ZnO photocatalysts was evaluated for the degradation of
169 Rhodamine B (RhB), Remazol Brilliant Blue R (RBBR) and Naproxen used at a 10 mg/L
170 concentration. Photodegradations were conducted under simulated solar light irradiation
171 (irradiance of 30 mW/cm^2 at 365 nm) at room temperature. Briefly, the CuO-Cu_2O/ZnO
172 heterostructures (30 mg) were dispersed in 30 mL of the pollutant solution and the mixture
173 was stirred in the dark in order to achieve adsorption-desorption equilibrium. After 60 min,
174 the solution was illuminated. Aliquots (1 mL) were withdrawn from the solution at regular
175 time intervals, centrifuged (4000 rpm for 5 min) to remove the photocatalyst and the
176 concentration of pollutant in the supernatant was monitored by UV-visible absorption
177 spectroscopy at 553, 590 and 229 nm for RhB, RBBR and Naproxen, respectively.
178 To identify the species involved in the photocatalytic degradation, DMSO, t-BuOH, NaN_3,
179 TEMPOL and EDTA were used to scavenge electrons, hydroxyl $^{\bullet}OH$ radicals, singlet oxygen
180 $^1O_2$, superoxide $O_2^{\bullet-}$ radicals and holes, respectively. The experimental procedure is similar
181 to that described above,, except that scavengers were added at a 10 mM concentration.
182
183 **3. Results and discussion**
184
185 3.1. Photocatalyst synthesis and characterization
186
187 ZnO NRs were prepared by hydrolysis of $Zn(OAc)_2$ under solvothermal conditions [4]. The
188 photodeposition of CuO-Cu_2O at the surface of ZnO NRs was conducted under ambient

conditions using $Cu(NO_3)_2$ as precursor in a water/ethanol (10:1) mixture and using a 150 W Xe lamp as light source (Fig. 1). Control experiments conducted in the absence of ZnO NRs show that pure CuO is produced in these experimental conditions as demonstrated by XRD (Fig. S1), which indicates that ZnO is involved in the formation of Cu_2O. The following mechanism can be proposed for the photodeposition of CuO-Cu_2O particles at the surface of ZnO NRs. At pH 9.5, OH^- ions react with $Cu(NO_3)_2$ to form the $Cu(OH)_4^{2-}$ complex unstable in water (eq. 1) which further decomposes into CuO (eq. 2). As the redox potential of the CuO/Cu_2O couple is of +0.6 V vs NHE [34], electrons photogenerated in the conduction band of ZnO partially reduce CuO into Cu_2O (eq. 3). Since TEM images do not show the deposition of separate CuO and Cu_2O particles on the ZnO surface (*vide infra*), the formation of core-shell CuO-Cu_2O particles could be considered.

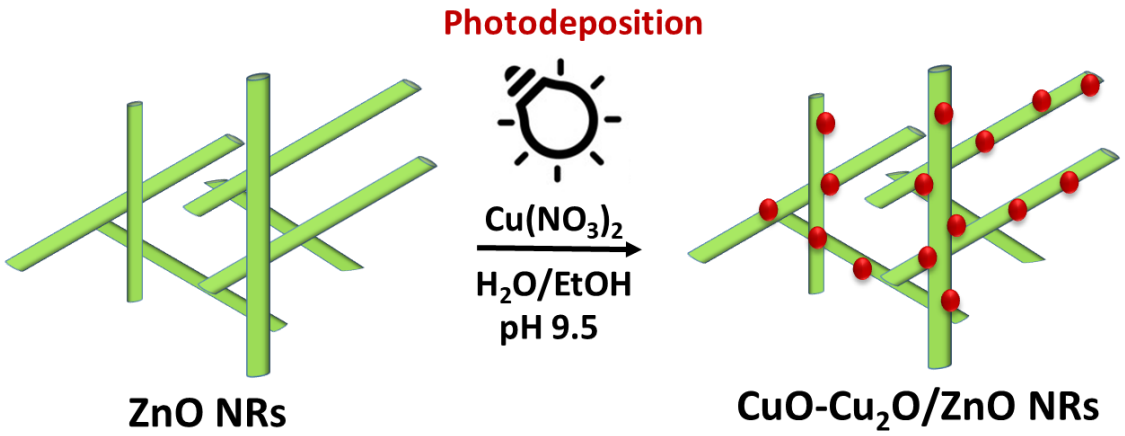

Fig. 1. Schematic representation of CuO-Cu_2O/ZnO photocatalysts synthesis.

$$Cu^{2+} + 4\ OH^- \longrightarrow Cu(OH)_4^{2-} \quad (1)$$

$$Cu(OH)_4^{2-} \longrightarrow CuO + 2\ OH^- + H_2O \quad (2)$$

$$2\ CuO + H_2O + 2e^- \longrightarrow Cu_2O + 2\ OH^- \quad (3)$$

XRD and Raman analyses were employed to characterize the phase structure and purity of the CuO-Cu_2O/ZnO nanohybrids obtained. The XRD analysis of ZnO and CuO-Cu_2O/ZnO particles indicates that all signals observed can be attributed to the wurtzite hexagonal phase of ZnO (Fig. 2a) (JCPDS No 36-1451). XRD peaks are sharp and well defined, suggesting the excellent crystalline quality of the samples. No diffraction peaks related to metallic Cu

oxides can be detected, which suggests that CuO-Cu_2O particles are of small size and highly dispersed on the surface of ZnO NRs. These results show that the coupling of ZnO with CuO-Cu_2O does not affect the crystalline structure of ZnO.

In the Raman spectra analysis of both ZnO and CuO-Cu_2O/ZnO samples (Fig. 2b), the most intense signal observed at 438 cm^{-1} corresponds to the characteristic *E2*(high) Raman mode of hexagonal ZnO. This signal can be attributed to the vibration of O atoms [35]. The weaker signal observed at 380 cm^{-1} can be attributed to the *A1*(TO) mode while the two signals at 204 and 329 cm^{-1} originate from the second-order Raman scattering of zone-boundary phonons (*2-TA*(M) and *2-E2*(M), respectively) [36]. The presence of these last two signals is indicative of an oxygen deficiency in ZnO NRs. The decrease in *E2*(high) signal intensity is linked to the decline in the crystallinity of ZnO and the stress induced by the deposition of CuO-Cu_2O on the ZnO NRs surface. Moreover, the marked shift observed in the peak positions for all ZnO-related Raman signals likely originates from the introduction of defect states in ZnO due to the formation of CuO-Cu_2O/ZnO nanohybrids.

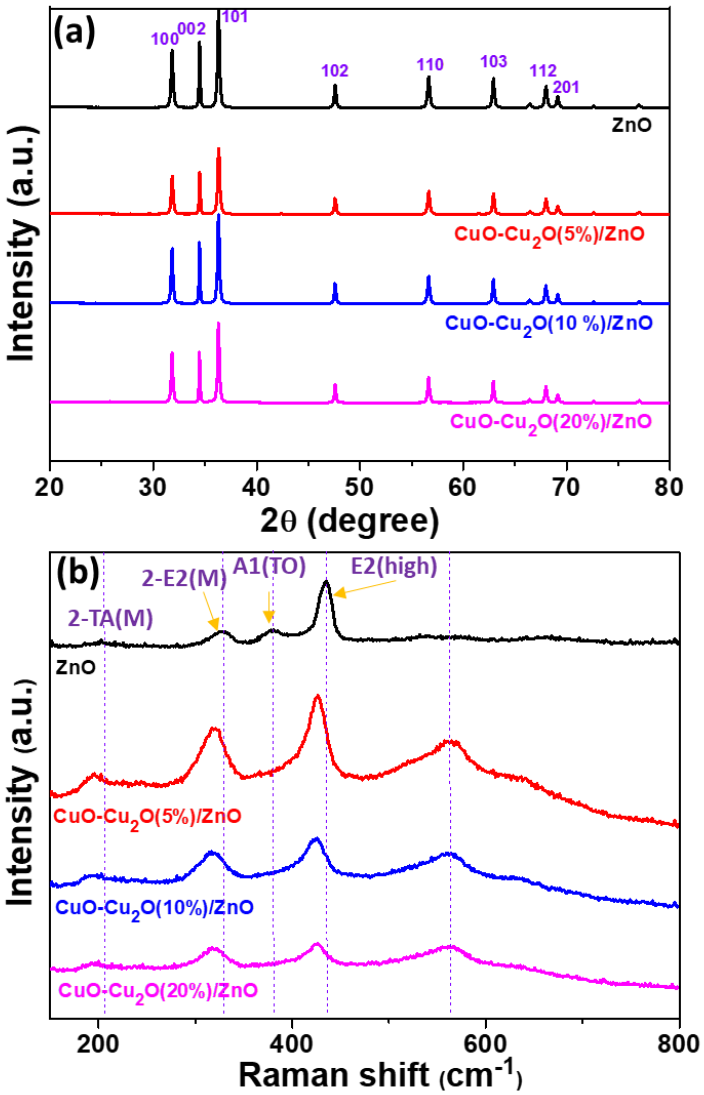

Fig. 2. (a) XRD patterns and (b) Raman spectra of ZnO NRs and CuO-Cu_2O/ZnO nanohybrids.

FT-IR was used to investigate the chemical functions present in the catalysts (Fig. 3). The weak and broad signal at ca. 3500 cm^{-1} corresponds to the O-H stretching of chemisorbed water molecules. Two signals can be observed at 1416 and 1344 cm^{-1} for both CuO-Cu_2O(10%)/ZnO and CuO-Cu_2O(20%)/ZnO nanohybrids. These peaks can be assigned to the symmetric stretchings of bidentate and bridged carbonate species [37] and suggest that CuO-Cu_2O particles favors the adsorption of CO_2 at the surface of ZnO as these signals are not observed for ZnO and CuO-Cu_2O(5%)/ZnO catalysts. The strong signals observed at 508 and 418 cm^{-1} can be attributed to Cu-O and Zn-O stretching vibrations.

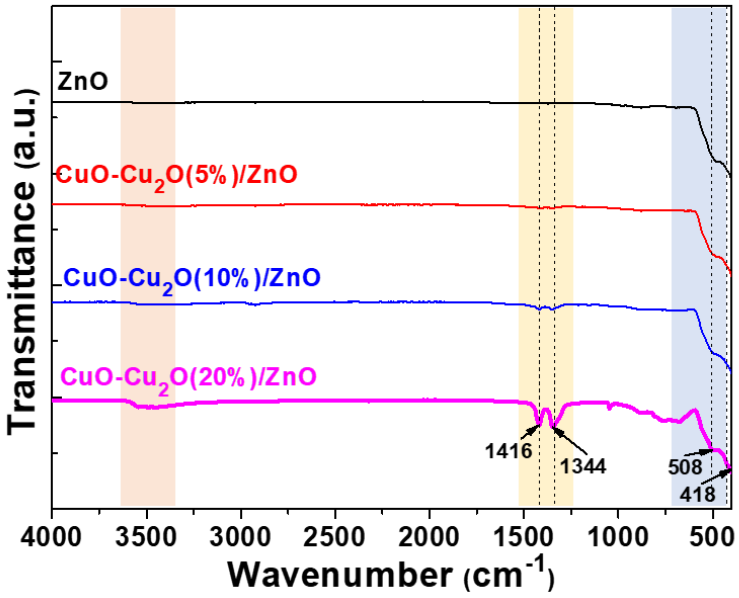

Fig. 3. FT-IR spectra of ZnO and CuO-Cu_2O/ZnO photocatalysts.

To gather additional insights into the surface composition and valence states of elements in the CuO-Cu_2O(10%)/ZnO nanohybrid, XPS measurements were performed. The survey spectrum shows only the presence of Zn, Cu, O and C elements, which confirms that the nanohybrid is pure (Fig. 4a). The C 1s peak likely originates from carbon adsorbed at the surface of the photocatalyst. The O 1s signal can be deconvoluted into four subpeaks located at 529.3, 530.3, 531.5 and 532.4 eV than can be assigned to Cu-O bonds, Zn-O bonds in the ZnO lattice, O in oxygen deficient regions and to organic O like carbonates, respectively (Fig. 4b). The Zn 2p peaks located at 1043.74 and 1021.3 eV can be assigned to Zn $2p_{1/2}$ and Zn $2p_{3/2}$ in the ZnO lattice, respectively. The binding energy difference of 22.44 eV confirms that Zn is in the +2 oxidation state (Fig. 4c) [24]. The Cu $2p_{3/2}$ peak can be deconvoluted into two signals located at 933.7 and 932.1 eV that can be assigned to Cu(+2) and Cu(+1) linked to O atoms, respectively (Fig. 4d) [38]. The presence of the three satellite peaks at 940.3, 941.7 and 943.4 eV confirms the presence of Cu in the +1 and +2 oxidation states [26].

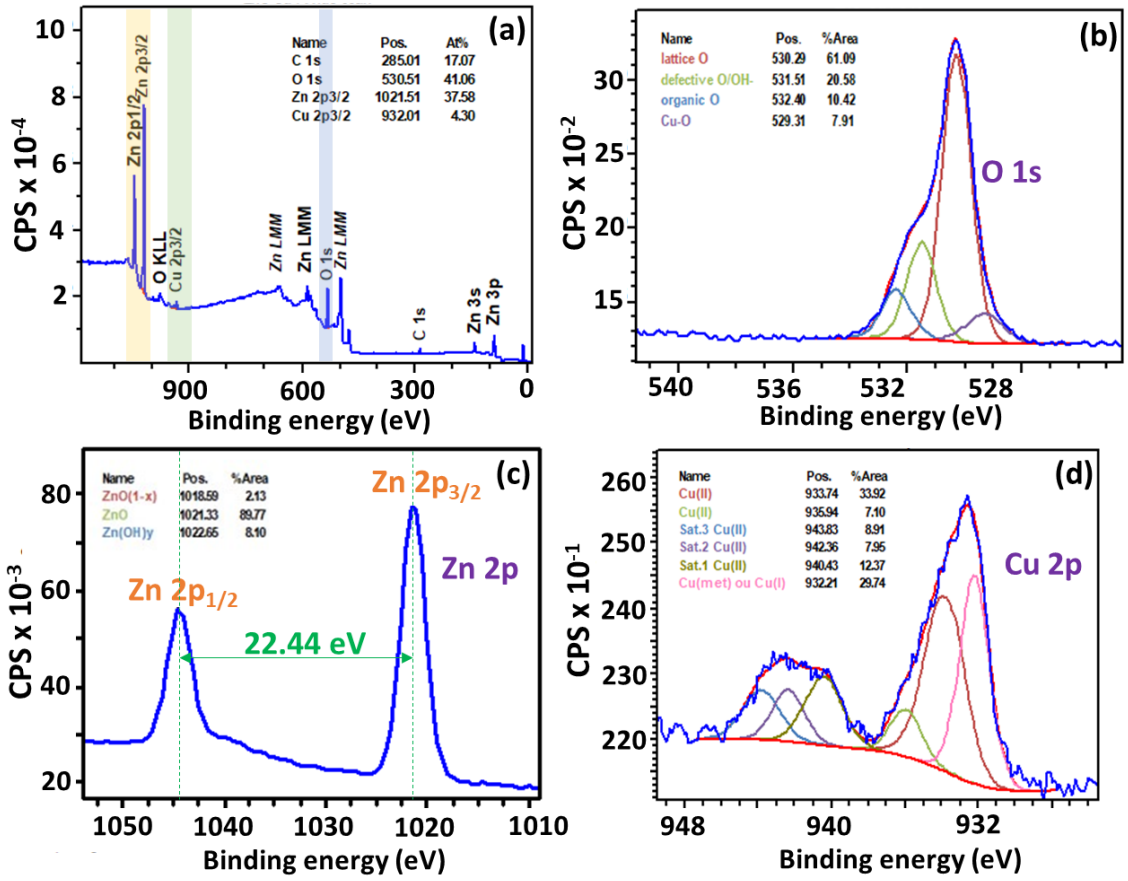

Fig. 4. (a) XPS overview spectrum and high resolution XPS spectra of (b) O 1s, (c) Zn 2p and (d) Cu 2p of the CuO-Cu_2O/ZnO nanohybrid.

The morphology and the composition of CuO-Cu_2O/ZnO catalysts were first examined by SEM and EDX. Fig. S2 shows that ZnO NRs and CuO-Cu_2O/ZnO catalysts self-assemble into microparticles with an average size of ca. 5 µm regardless of the amount of CuO/Cu_2O deposited on the surface of ZnO. The EDX spectrum of the CuO-Cu_2O(10%)/ZnO sample selected as representative shows the presence of Zn, Cu and O elements (Fig. S3).

The morphology and the particle size of ZnO NRs and CuO-Cu_2O/ZnO catalysts were further evidenced by TEM and HR-TEM. The average length of ZnO NRs is of ca. 150 nm and their diameter of 35 nm, which corresponds to an aspect ratio of 4.3 (Fig. 5a). The lattice planes separation is of 0.29 nm, value corresponding to the (100) planes of wurtzite ZnO, which agrees well with XRD results. The selected area electron diffraction (SAED) pattern further confirms the hexagonal structure of ZnO (inset of Fig. 5b). At the surface of ZnO NRs, small pseudo-spherical nanoparticles of CuO-Cu_2O with an average diameter of 2.4 ± 1.3 nm could be observed (Fig. 5b-d). The interplanar spacing is of 0.25 nm, which corresponds to the

(002) planes of monoclinic CuO (JCPDS No 03-065-2309). The EDS mapping images confirm that Zn, O and Cu elements are homogeneously distributed in the CuO-Cu_2O/ZnO nanohybrid (Fig. 5e-h). These results demonstrate the successful formation of a p-n heterojunction between ZnO NRs and CuO-Cu_2O nanoparticles, which is beneficial for the separation of photogenerated charge carriers.

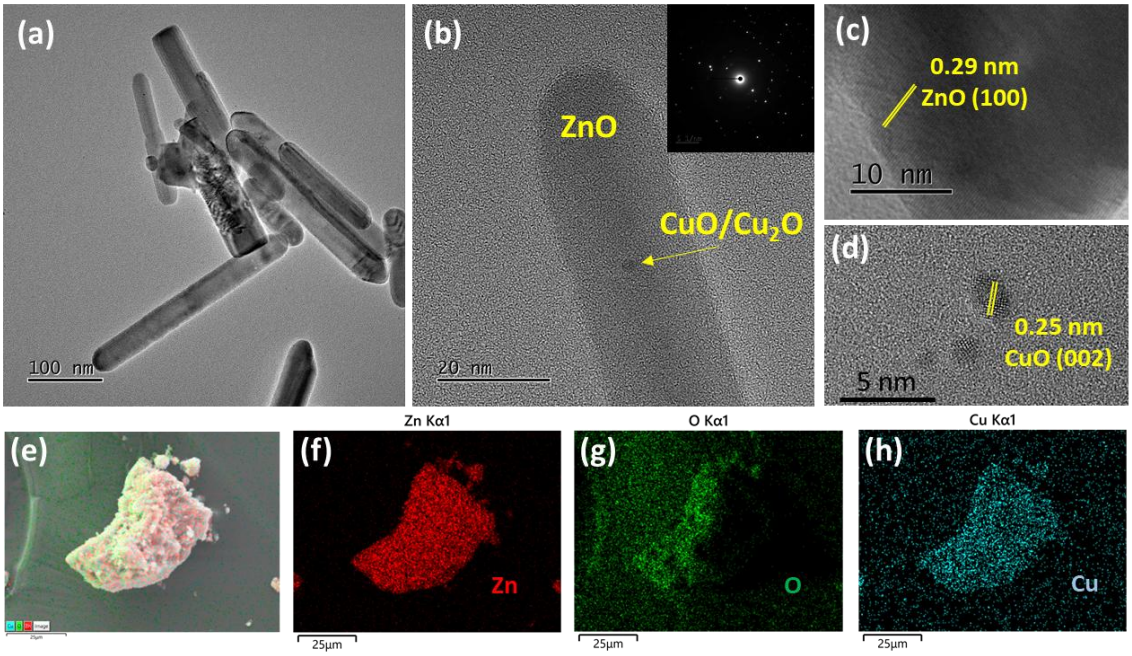

Fig. 5. (a-d) TEM and HR-TEM images of the CuO-Cu_2O(10%)/ZnO sample. The inset of b is the SAED pattern. (e) SEM image and (f-h) Zn, O, and Cu elemental mapping images of the CuO-Cu_2O(10%)/ZnO nanohybrid.

UV-visible absorption spectra were used to study the optical absorption processes in ZnO and CuO-Cu_2O/ZnO photocatalysts. The absorption onset of ZnO NRs is located at 392 nm (Fig. 6a) and the bandgap absorbance at ca. 362 nm. The bandgap energy *Eg* was determined using the Tauc plot $(\alpha h\gamma)^n$ = A ($h\gamma$-*Eg*) where α is the absorption coefficient, *h* the Planck constant, γ the frequency of incident photon and A a constant. The value of n depends on the nature of the optical transition and is equal to 1/2 for the CuO-Cu_2O/ZnO photocatalyst as ZnO, CuO and Cu_2O are direct bandgap semiconductors. $(\alpha hv)^{1/2}$ was plotted versus hv and the linear portion of the plot was extrapolated to the ordinate as shown in Fig. 6b. The bandgap energy *Eg* of ZnO is estimated to be of 3.16 eV. After coupling of ZnO with CuO-Cu_2O, the visible and near infrared absorption markedly increases which is

beneficial for producing more photogenerated charge carriers under solar light illumination. For CuO-Cu_2O/ZnO sample, two absorption signals can be observed at 451 and 477 nm (Fig. 6a). *Eg* values derived from these signals are of 2.39 and 2.18 eV and could be associated to Cu_2O and CuO, respectively, as CuO exhibits a weaker bandgap than Cu_2O (Fig. 6c) [39,40]. The bandgap energies determined for CuO and Cu_2O are larger than those of the bulk materials (1.85 and 2.0-2.2 eV for CuO and Cu_2O, respectively), which confirms the nanosize of these particles and their quantum confinement. A decrease of the bandgap energy is observed for CuO-Cu_2O/ZnO nanohybrids (3.12, 3.08 and 3.04 eV for ZnO associated to 5, 10 and 20% CuO-Cu_2O, respectively), which is indicative of new bonds formed between ZnO and CuO-Cu_2O and thus of the close interfacial contact and coupling between these nanoparticles to form CuO-Cu_2O/ZnO heterojunctions [41,42].

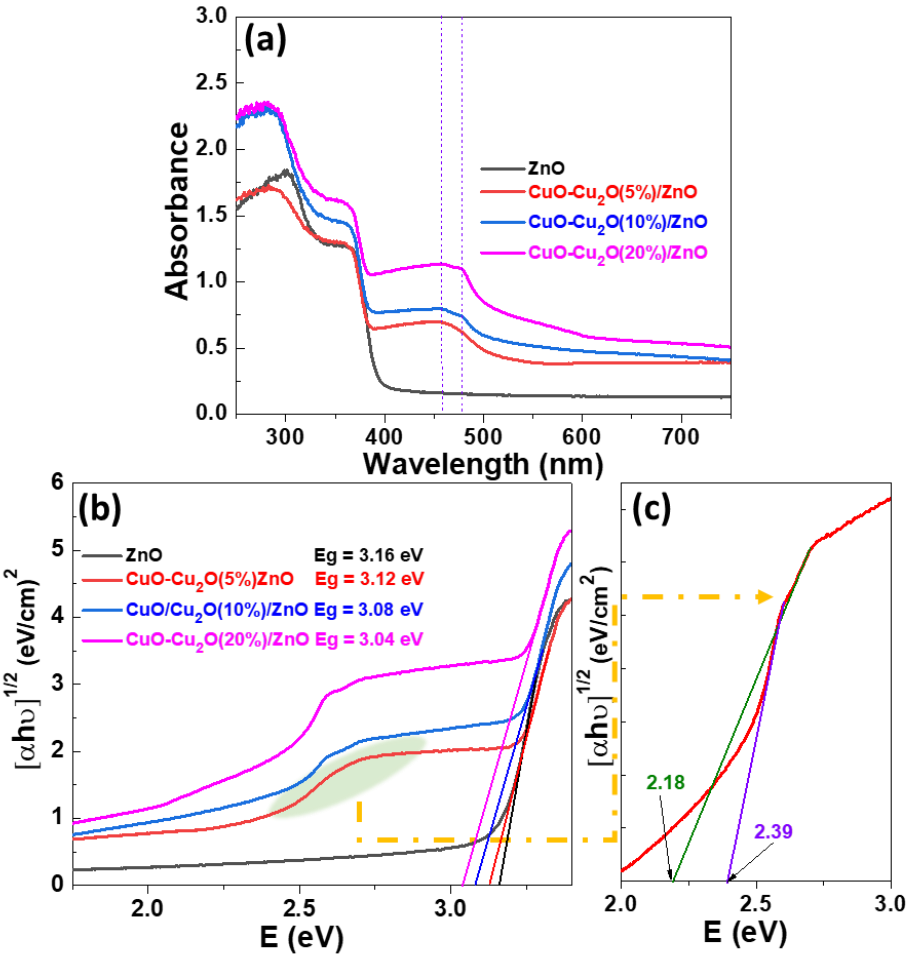

Fig. 6. (a) UV-visible absorption spectra, (b) the corresponding Tauc plots of ZnO and CuO-Cu_2O/ZnO samples. (c) Magnification of 2.0-3.0 eV zone for the CuO-Cu_2O(5%)/ZnO photocatalyst used to determine the energy bandgap of CuO and Cu_2O.

To study the dynamics of the photogenerated charge carriers in ZnO and CuO-Cu_2O/ZnO catalysts, PL emission and EIS measurements were conducted. The room temperature PL emission spectra of ZnO NRs and CuO-Cu_2O/ZnO nanohybrids are shown in Fig. 7a. All samples exhibit a near-band-edge (NBE) PL emission located at 385 nm (3.22 eV) and a weaker and broad PL emission in the visible region. The NBE emission originates from the excitonic recombination while the visible emission is linked to various defect states including oxygen and zinc vacancies and oxygen and zinc interstitials [43,44]. Upon deposition of 5 or 10% CuO-Cu_2O nanoparticles on ZnO NRs, both the NBE and the visible PL emissions decrease, indicating that the recombination of photogenerated electrons in the conduction band (CB) with the holes in the valence band (VB) is reduced. This improved separation of charge carriers is favorable for the photocatalytic activity. A slight red-shift of the NBE emission from 385 to 391 nm can also be observed, which agrees well with UV-visible absorption spectra and the decrease of the bandgap energy observed for CuO-Cu_2O/ZnO nanohybrids. For the CuO-Cu_2O(20%)/ZnO sample, a significant increase of the defect-related emission is observed, suggesting that the charge carrier separation is decreased in this nanohybrid.

The interface charge separation efficiency of photogenerated electrons and holes is a key parameter affecting the photocatalytic activity and was investigated using EIS Nyquist plots (Fig. 7b). As can be seen, the arc radius of the CuO-Cu_2O(10%)/ZnO nanohybrid is the smallest indicating a lower interface layer resistance and a faster interfacial charge transfer. These results show that the heterojunction between ZnO and CuO-Cu_2O particles allows to improve the separation and the transfer of charge carriers. The fitting results were obtained using the equivalent circuit depicted in the inset of Fig. 7b and the charge transfer resistance R_{CT} was determined (R_S is the resistance of the electrolyte, CPE is the constant phase element and W is the Warburg impedance). As seen in Table S1, the lowest value of R_{CT} was observed for the CuO-Cu_2O(10%)/ZnO nanohybrid, further confirming that CuO-Cu_2O nanoparticles photodeposited on ZnO NRs allow an improved charge separation and an efficient charge transfer.

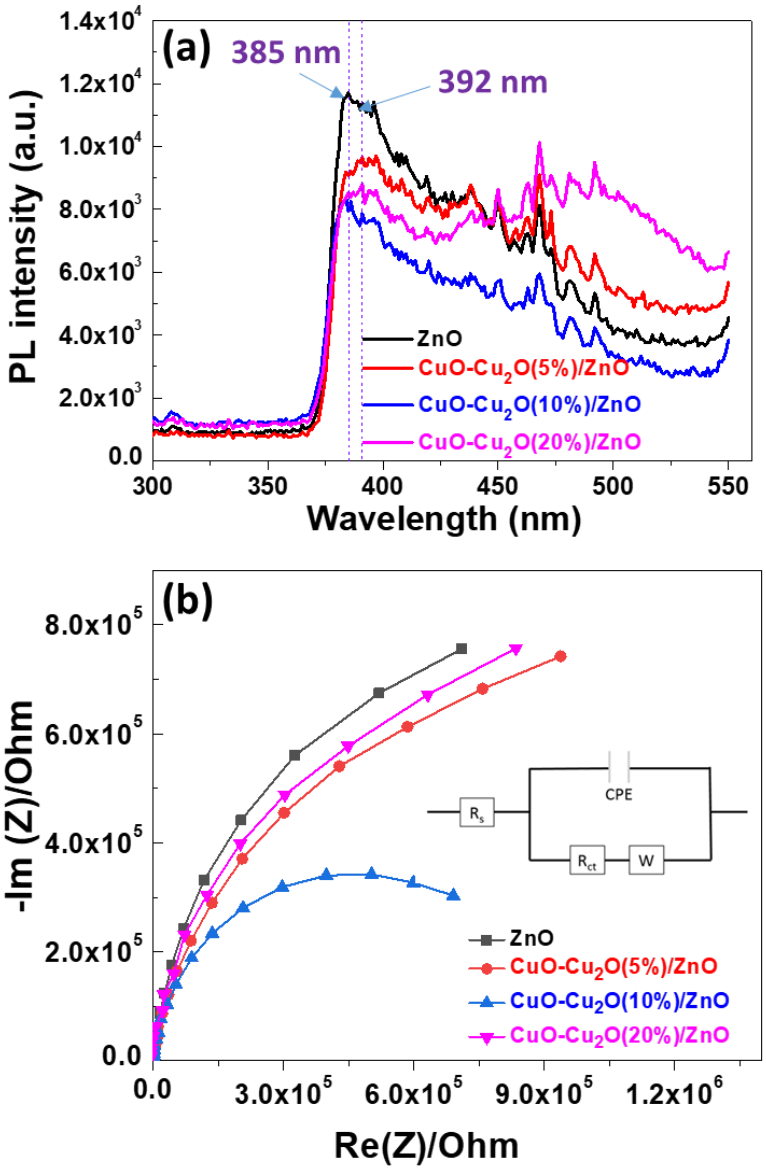

Fig. 7. (a) PL emission spectra recorded after excitation at 290 nm and (b) EIS responses of ZnO and CuO-Cu_2O/ZnO samples (the inset is the equivalent circuit used to fit EIS curves).

3.2. Photocatalytic activity: degradation of RhB, RBBR and Naproxen and influence of the pH and of salts

The amount of pollutant adsorbed at the surface of the photocatalyst is a key parameter influencing the photocatalyst performance. In this context, the point of zero charge (pzc) of the photocatalyst is of great importance. Since the adsorption of the pollutant occurs on the photocatalyst surface, the efficiency of the photocatalyst depends both on the pH and on

the charge of the pollutant. The pzc of ZnO NRs is of 9.2. Upon deposition of 10% CuO-Cu_2O nanoparticles on the surface of ZnO NRs, a decrease of the pzc to 8.1 is observed (Fig. S4), indicating that the surface of the CuO-Cu_2O(10%)/ZnO catalyst is negatively charged at pH values higher than 8.1 and positively charged below 8.1.

The photocatalytic activity of ZnO NRs and of CuO-Cu_2O/ZnO heterojunctions was first evaluated under simulated solar light irradiation (light irradiance of 30 mW/cm^2) for the degradation of a cationic (Rhodamine B, RhB) and an anionic (Remazol Brilliant Blue R, RBBR) dye used at a 10 mg/L concentration and at pH 7. Preliminary experiments showed that less than 3% of these dyes are bleached under these illumination conditions in the absence of photocatalyst. As can be seen from Fig. 8a, RhB weakly adsorbs on the surface of ZnO and CuO-Cu_2O/ZnO photocatalysts (less than 5%) during the 60 min of stirring in the dark due to the electrostatic repulsion between the positively-charged dye and the positively-charged photocatalyst. As soon as light is turned on, a fast photodegradation of the dye is observed. The highest photocatalytic activity is observed for the CuO-Cu_2O(10%)/ZnO photocatalyst (full degradation after ca. 50 min of illumination), which agrees well with PL and EIS results and confirms that the charge carrier separation is the highest for this nanohybrid (see Fig. S5a for UV-visible absorption spectra). The photodegradation of RhB follows a pseudo-first-order reaction and the rate constant of the photodegradation was determined using the equation $\ln(C_0/Ct) = kt$ where C_0 and C are the initial concentration and the residual concentration at time t of RhB, respectively, and k is the apparent first-order rate constant. After linear regression, the slope of the plot of $\ln(C_0/C)$ vs time equals k. The k values determined for ZnO and ZnO coupled to 5, 10 and 20% CuO-Cu_2O are 0.0653, 0.0806, 0.0846 and 0.0802 min^{-1}, respectively, which confirms that CuO-Cu_2O(10%)/ZnO is the photocatalyst exhibiting the highest activity (Fig. S6).

As expected, at pH 7, the negatively-charged RBBR dye strongly adsorbs on CuO-Cu_2O(10%)/ZnO photocatalyst (ca. 70%) but less on ZnO, suggesting a strong association of CuO-Cu_2O nanoparticles with the dye (Fig. 8b and S5b). During the photodegradation of RBBR, small amounts of photocatalyst was taken at different reaction times, dried and analyzed by UV-visible absorption and FT-IR spectroscopy (Fig. S7). Results obtained show that all RBBR adsorbed and in solution is photodecomposed in less than 90 min using the CuO-Cu_2O(10%)/ZnO photocatalyst.

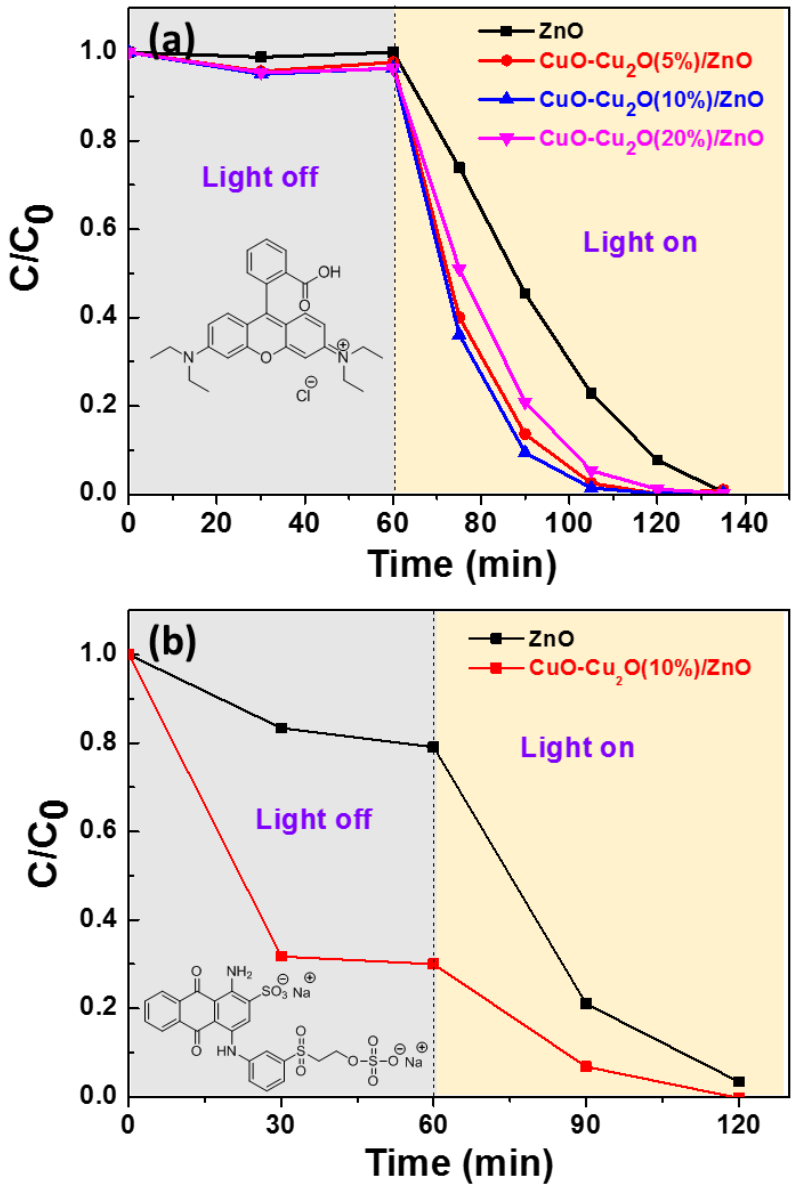

381

382 **Fig. 8**. Time course study of the (a) RhB and (b) RBBR photocatalytic degradation by ZnO and
383 CuO-Cu_2O/ZnO nanohybrids under simulated solar light irradiation.

384

385 Naproxen is a non-steroidal anti-inflammatory drug belonging to the 2-arylpropionic class
386 and is widely used not only to cure injuries and pains but also as anticancer and
387 antimicrobial agent. Naproxen has been identified as an emerging contaminant and is
388 present at concentration up to 32 µg/L in groundwater, rivers and even tap water [45,46].
389 Thus, the development of efficient methods to degrade Naproxen from contaminated water
390 has gained high interest in recent years (Table S2). The photocatalytic activity of CuO-
391 Cu_2O/ZnO nanohybrids was evaluated for the degradation of Naproxen under simulated

392 solar light irradiation. The intensity of the UV-visible absorption signal of Naproxen at 229
393 nm did not change when irradiating this compound in the absence of the photocatalyst,
394 indicating that the photolysis is negligible. The CuO-Cu_2O(10%)/ZnO catalyst is the more
395 efficient for the degradation of Naproxen and a quantitative decomposition is reached after
396 ca. 75 min irradiation (Fig. 9a). The k values determined for ZnO and 5, 10 and 20% CuO-
397 Cu_2O modified ZnO are 0.0167, 0.0219, 0.0363 and 0.0222 min^{-1} (Fig. S8), further confirming
398 that the CuO-Cu_2O(10%)/ZnO heterostructured photocatalyst can markedly improve the
399 photodegradation of Naproxen. Monitoring of photodegradation by UV-visible spectroscopy
400 shows that new signals appear at 260 and 315 nm after 15 and 30 min irradiation, likely due
401 to the hydroxylation of the naphthalene moiety by the active species generated during the
402 photocatalytic treatment as previously observed using TiO_2 nanoparticles as photocatalyst
403 (Fig. 7b)[47]. As the mineralization of organic pollutants is crucial for wastewater treatment,
404 the total organic carbon (TOC) removal efficiency of Naproxen over the CuO-Cu_2O(10%)/ZnO
405 catalyst reached 58% after 120 min irradiation, further confirming that the photocatalyst can
406 effectively mineralize Naproxen. The influence of pH during the photodegradation of
407 Naproxen was also investigated (Fig. 9c). Photodegradation is very effective at pH 6, 7 or 8
408 and is only slightly slowed down at pH 10. A marked slowdown of the photodegradation rate
409 is observed at pH 4 and pH 12. Table S2 describes the performance of various catalysts
410 developed in recent years for Naproxen photodegradation. Even if the irradiation conditions
411 or catalyst amounts are not identical to that used in this study, the results show that the
412 CuO-Cu_2O(10%)/ZnO catalyst is among the most effective for the photodegradation of
413 Naproxen.
414 The stability and the recyclability of a photocatalyst are key parameters for assessing its
415 practical applicability for real water decontamination. Fig. 9d shows that the performance of
416 the CuO-Cu_2O(10%)/ZnO catalyst for the degradation of Naproxen is not impaired after 9
417 recyclings. The stability of the photocatalyst was also evaluated for the degradation of RhB
418 and no decrease in activity was observed after five recycling (Fig. S9). These results
419 demonstrate that there is no blocking of the active sites by the intermediates or by
420 Naproxen or RhB. FT-IR and XRD analyses were performed to identify the changes in surface
421 chemistry and crystallinity that may have taken place after repeated use for the degradation
422 of Naproxen (Fig. S10a-b). The only changes observed on the FT-IR are the appearance of a
423 weak signals at ca. 2910 cm^{-1} corresponding to C-H stretching and between 1200 and 1148

cm^{-1} that may be assigned to C-O stretching (Fig. S10a). The crystallinity of the catalyst is not affected by its multiple reuses (Fig. S10b). SEM images of the freshly prepared catalyst and the reused catalyst also show that no particle agglomeration takes place (Fig. S10c-d).

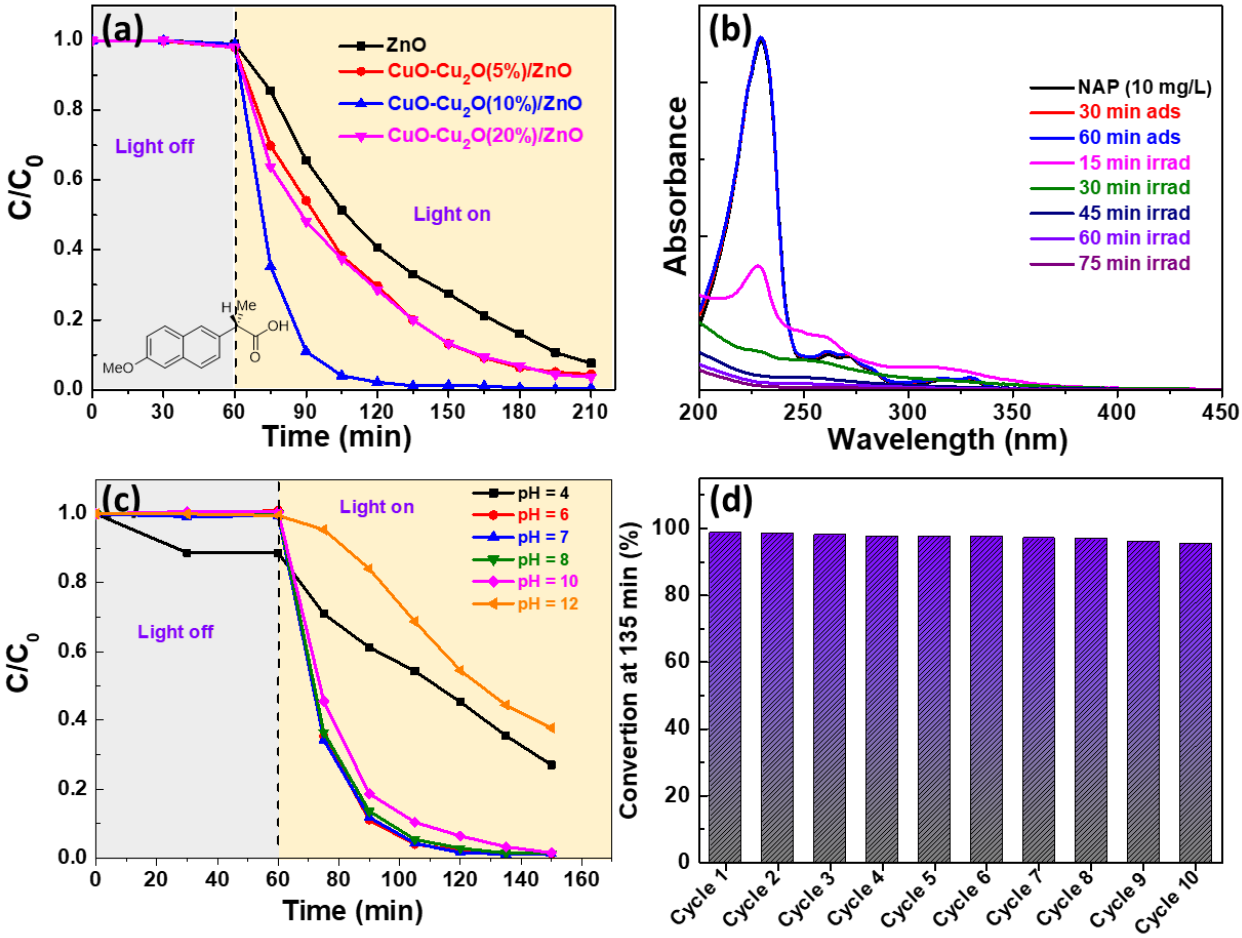

Fig. 9. (a) Photocatalytic activity of ZnO and CuO-Cu_2O/ZnO catalysts for the Naproxen degradation, (b) UV-visible absorption spectra of Naproxen photodegradation using the CuO-Cu_2O(10%)/ZnO photocatalyst, and (c) influence of pH for the photodegradation of Naproxen using the CuO-Cu_2O(10%)/ZnO catalyst. (d) Stability experiments for Naproxen photodegradation by the CuO-Cu_2O(10%)/ZnO catalyst under simulated solar light irradiation.

As natural water matrix may contain various kinds of ions in solution with the pollutant, the photodegradation of Naproxen was evaluated in commercial mineral water containing calcium (240 mg/L), magnesium (42 mg/L), sodium (5.2 mg/L), sulfate (400 mg/L), hydrogenocarbonate (384 mg/L), nitrate (4.4 mg/L) and pH 7.6. Fig. 10a shows that the rate

of Naproxen photodegradation is only slightly affected by the presence these ions. Naproxen is decomposed by 97% after 60 min irradiation in ultrapure water and by 93% in mineral water after the same period.

To further evaluate the influence of inorganic salts on the photocatalytic efficiency, additional experiments were conducted using NaCl, NaH_2PO_4, Na_2HPO_4, Na_2SO_4, $CaCl_2$ and $MgCl_2$ used at a 5.10^{-3} M concentration (Fig. 10b). Except NaH_2PO_4 which causes a pH drop to 4, all other salts do not influence the pH which remains close to 7. No significant decrease in the photocatalytic efficiency was observed in the presence of NaCl, Na_2SO_4, $CaCl_2$ or $MgCl_2$, indicating that these salts have no scavenging effect towards the CuO-Cu_2O(10%)/ZnO catalyst. A slight decrease of the photocatalytic efficiency is observed when adding Na_2HPO_4 (ca. 85% degradation after 60 min irradiation). The strongest inhibition of the photodegradation of Naproxen (ca. 10% degradation after 60 min) is observed when adding NaH_2PO_4. This decrease of the photocatalytic efficiency is probably related to the decrease in pH but a competition between the adsorption of NaH_2PO_4 and Naproxen at the surface of the photocatalyst or the scavenging effect of $H_2PO_4^-$ ions towards reactive oxygen species like hydroxyl $^{\bullet}OH$ radicals or holes h^+ [48].

The photodegradation of a mixture of Naproxen and RhB, both used at a 10 mg/L concentration in the absence of inorganic ions, was also investigated. Naproxen and RhB show UV-visible absorption maxima at 229 and 553 nm, respectively, which were used to determine the concentrations of these compounds in the mixture (Fig. 10c). Although Naproxen has a higher affinity for the CuO-Cu_2O(10%)/ZnO catalyst surface due to its negative charge, both Naproxen and RhB were efficiently decomposed, indicating non-interference of pollutants adsorption at the surface of the photocatalysts followed by their degradation. Naproxen and RhB are decomposed to 94 and 100% after 70 min irradiation (Fig. 10d). Moreover, a synergistic enhancement in the photodegradation rate is observed. The pseudo-first-order rate constants k when decomposing the mixture are 0.0480 and 0.0961 min^{-1} for Naproxen and RhB, respectively (Fig. S11), while k values are 0.0363 and 0.0846 min^{-1} for Naproxen and RhB, respectively, when the photodegradation is carried out on each of the pollutants taken separately. We assume that this synergy may originate from an electrostatic attraction between Naproxen and RhB and the synchronously consumption of electron and holes (or the reactive oxygen species derived) which allows to decrease the electron-hole recombination and thus enhance the photocatalytic activity [49].

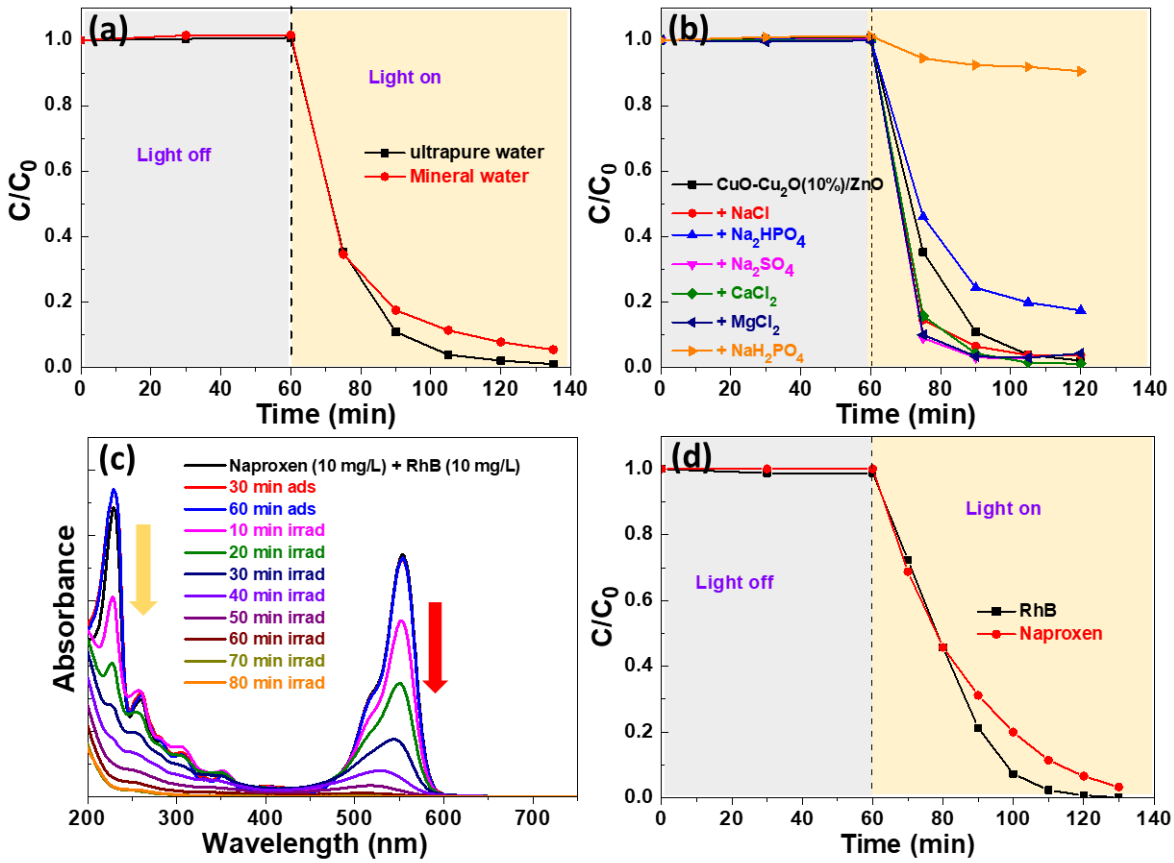

Fig. 10. (a) Photodegradation of Naproxen using the CuO-Cu_2O(10%)/ZnO catalyst (a) in ultrapure water and mineral water (b) in the presence of salts. (c) UV-visible absorption spectra of Naproxen and RhB during their photocatalytic degradation using the CuO-Cu_2O(10%)/ZnO catalyst, (d) Photocatalytic activity of the CuO-Cu_2O(10%)/ZnO catalyst during the simultaneous degradation of Naproxen and RhB. All experiments were conducted under simulated solar light irradiation (irradiance of 30 mW/cm^2).

The photocatalytic degradation of Naproxen was investigated by LC UV/(+) MS2 and some of the intermediates identified during the first-half-hour of the reaction are depicted in Fig. 11 (see Fig. S12 and Table S3 for HPLC-UV chromatograms and MS analyses). Upon irradiation in the presence of the CuO-Cu_2O(10%)/ZnO catalyst, a dihydroxylation of Naproxen is quickly observed and leads to compound **2** (262 Da). Intermediates that may correspond to (*S*)-2-naphthalen-2-yl) propenoic acid **1** (200 Da) and to 1-(6-methoxynaphthalen-2-yl) ethanone **4** (200 Da) were observed but, on the basis of studies described in the literature [50-52], the formation of the intermediate **4** resulting from the oxidation of the carbon-carbon double

bond of **3** seems more likely. Compound **4** is further dihydroxylated to produce **5** (232 Da). 2-Methoxy-6-vinylnaphthalene **3** (184 Da) originating from the decarboxylation of Naproxen followed by the loss of a proton is also detected at the beginning of the reaction. Products **7** (234 Da) originating from the hydroxylation of the carbon-carbon double bond and the dihydroxylation of the naphthalene moiety and dihydroxylated compound **6** were also detected. Products **2**, **5**, **6** and **7** are further oxidized by the reactive species generated by the irradiation of the CuO-Cu_2O/ZnO (10%) photocatalyst, which leads to the mineralization of Naproxen.

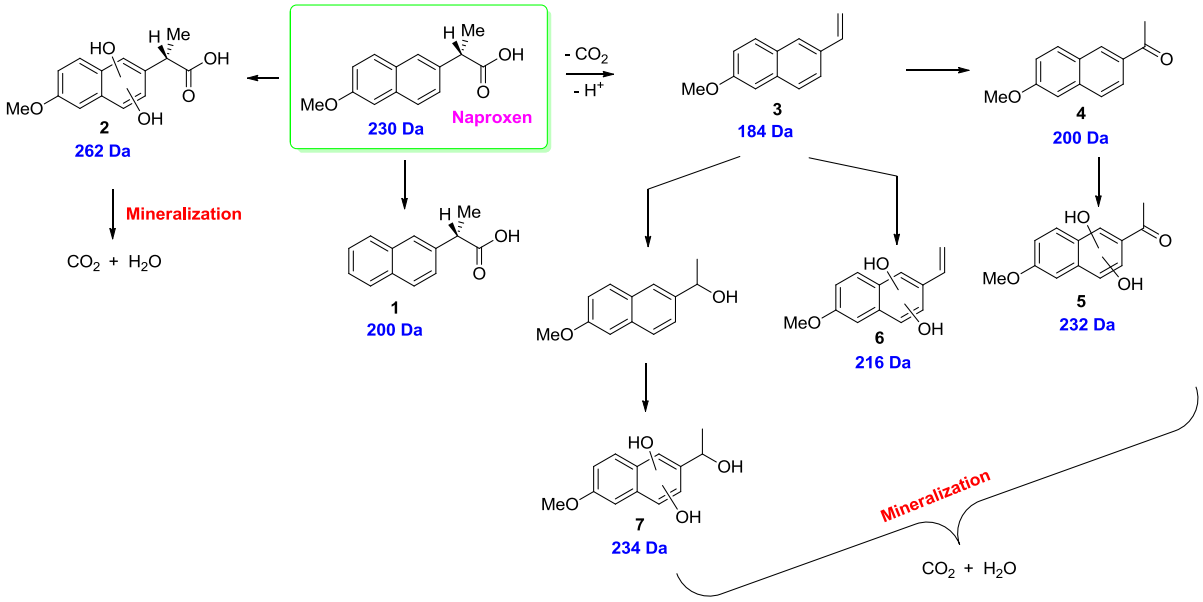

Fig. 11. Structure of Naproxen photodegradation products identified by LC-UV-MS and MS2.

3.3. Photocatalytic mechanism

To gain an insight into the photocatalytic mechanism, scavenging experiments were conducted using TEMPOL, NaN_3, DMSO, t-BuOH and EDTA to capture $O_2^{\bullet-}$ radicals, singlet oxygen $^1O_2$, electrons, $^{\bullet}$OH radicals and holes, respectively (Fig. 12a). As can be seen, $O_2^{\bullet-}$ radicals, $^1O_2$ and especially holes are the main species involved in the degradation of Naproxen (the photodegradations are reduced to 15, 27 and 5% after 75 min irradiation when experiments are conducted in the presence of TEMPOL, NaN_3 and EDTA, respectively, while in the absence of a scavenger, the conversion is 97%). Electrons and $^{\bullet}$OH radicals are also involved in the photodegradation but much weaker (the photodegradations remain of 66 and 78% when adding DMSO and t-BuOH, respectively).

Assessing the band edge positions and the band alignment of CuO, Cu_2O and ZnO is of paramount importance to understand both the charge transfers at the heterojunction as well as the formation mechanisms of species involved in the photodegradation. The positions of the valence band (VB) and of the conduction band (CB) of CuO, Cu_2O and ZnO were determined using equations (1) and (2) :

$$E_{VB} = \chi - E^e + 0.5\,Eg \qquad (1)$$

$$E_{CB} = E_{VB} - Eg \qquad (2)$$

where E_{VB} is the VB potential and E_{CB} the CB potential, χ is the absolute electronegativity of the semiconductor (5.33, 5.81 and 5.89 for Cu_2O, CuO and ZnO, respectively), Eg is the bandgap energy determined from UV-visible DRS (3.08 eV for the CuO-Cu_2O/ZnO nanohybrid), and E^e is the energy of free electrons on the hydrogen scale (ca. 4.5 eV) [53].

Using these data, the following mechanism can be proposed (Fig. 12b). Under sunlight irradiation, electrons located in the VBs of CuO, Cu_2O and ZnO are promoted to the CBs leaving holes in the VBs. These holes can directly oxidize Naproxen into $[Naproxen]^+$ as holes were demonstrated to play the major in the photodegradation mechanism. The holes in the VB of ZnO may also oxidize water molecules adsorbed at the surface of the photocatalyst into $^{\bullet}OH$ radicals but these radicals play only a minor role in the decomposition of Naproxen.

Only electrons promoted in the CB of Cu_2O can reduced O_2 molecules on the catalyst surface into $O_2^{\bullet-}$ radicals that have been identified as playing a major role in the photodegradation. After contact, the Fermi level of Cu_2O and ZnO equilibrates due to the formation of the p-n heterojunction, which modifies the band positions. Thus, due to the very small energy gap between of CB potential of ZnO (-0.15 eV vs NHE) and the $O_2/O_2^{\bullet-}$ couple (-0.33 eV vs NHE), it is likely that photogenerated electrons in the CB of ZnO may also be involved in the production of $O_2^{\bullet-}$ radicals.

The electrons in the CB of ZnO can also migrate to the CB of CuO due to the p-n heterojunction between ZnO and CuO. Next, the electrons accumulated in the CB of CuO can scavenge holes in CuO via a Z-scheme mechanism. Holes in CuO and ZnO can also transfer to the VB of Cu_2O.

Holes in CuO, ZnO and Cu_2O may also be consumed by $O_2^{\bullet-}$ radicals (eq. (3)), thus allowing the production of $^1O_2$ which is a key species involved in the photodegradation mechanism.

$$O_2^{\bullet-} + h^+ \rightarrow {}^1O_2 + {}^3O_2 \qquad (3)$$

All these charge transfer favor the charge separation and thus the photocatalytic activity. Moreover, the fast consumption of holes by reaction with the pollutant or via charge transfer allows to increase the stability of the CuO-Cu_2O (10%)/ZnO photocatalyst toward photocorrosion.

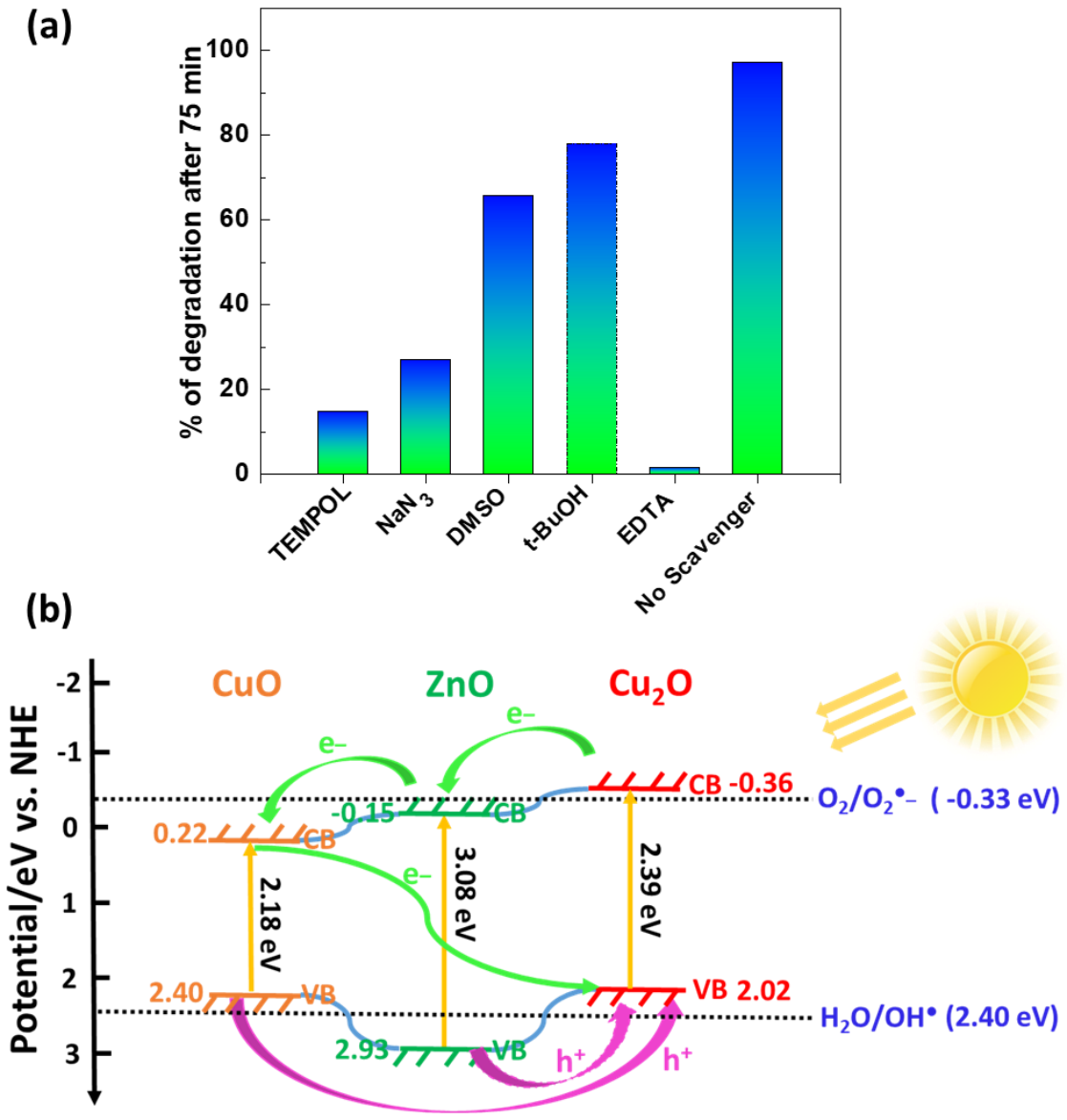

Fig. 12. (a) Photodegradation of Naproxen using the CuO-Cu_2O (10%)/ZnO catalyst in the presence of reactive species trapping compounds used at a 10 mM concentration and (b) Schematic representation of the charge transfers in the CuO-Cu_2O (10%)/ZnO heterostructured photocatalyst under solar light illumination.

4. Conclusion

In summary, p-n CuO-Cu_2O/ZnO heterostructured photocatalyts were prepared via a facile and green photodeposition route and successfully used for the degradation of anionic and cationic dyes (RhB, RBBR) and Naproxen under simulated solar light irradiation. The structural characterizations show that the photodeposition route allows the association of ca. 2.4 nm-sized CuO-Cu_2O particles of monoclinic structure with wurtzite ZnO nanorods. The high photocatalytic performance of the CuO-Cu_2O(10%)/ZnO photocatalyst originates both from the p-n heterojunction which allows to expand the visible light absorption and from the decreased recombination rate of photogenerated charge carriers. Its high performance combined with its high stability make the CuO-Cu_2O(10%)/ZnO photocatalyst of high potential for environmental remediation.

CRediT authorship contribution statement

Mouna Ibn Mahrsi: Methodology, Investigation, Data curation, Writing – original draft. **Bilel Chouchene**: Methodology, Investigation, Data curation, Writing – original draft. **Thomas Gries**: Investigation, Data curation, Writing – original draft. **Vincent Carré**: Investigation, Data curation, Writing – original draft. **Ghouti Medjahdi**: Methodology, Investigation, Data curation. **Fadila Ayari:** Supervision, Review – original draft. **Lavinia Balan**: Investigation, Data curation, Writing – original draft. **Raphaël Schneider**: Supervision, Conceptualization, Writing – review & editing, Funding acquisition.

Declaration of Competing Interest

The authors declare that they have no known competing financial interests or personal relationships that could have appeared to influence the work reported in this paper.

Acknowledgments

This project has benefited from the expertise and the facilities of the Platform MACLE-CVL which was co-funded by the European Union and Centre-Val de Loire Region (FEDER). The authors acknowledge Dr Khalid Ferji (LCPM, Université de Lorraine) for Zeta potential analysis.

Appendix A. Supplementary data

584 Supplementary material related to this article can be found, in the online version, at
585 doi:https://
586
587 **References**
588
589 [1] H. Liu, C. Wang, G. Wang. Photocatalytic Advanced Oxidation Processes for Water
590 Treatment: Recent Advances and Perspective. Chem. Asian J. 2020, 15, 3239–32.
591 [2] F.H. Abdullah, N.H.H. Abu Bakar, M. Abu Bakar, Current advancements on the fabrication,
592 modification, and industrial application of zinc oxide as photocatalyst in the removal of
593 organic and inorganic contaminants in aquatic systems. J. Hazard. Mater. 424 (2022) 127416.
594 [3] C. Boon Ong, L. Yong Ng, A. Wahab Mohammad. A review of ZnO nanoparticles as solar
595 photocatalysts: Synthesis, mechanisms and applications. Renew. Sust. Energ. Rev. 81 (2018)
596 536-551.
597 [4] H. Moussa, E. Girot, K. Mozet, H. Alem, G. Medjahdi, R. Schneider. ZnO rods/reduced
598 graphene oxide composites prepared via a solvothermal reaction for efficient sunlight-driven
599 photocatalysis. Appl. Catal. B: Environ. 185 (2016) 11-21.
600 [5] F. Achouri, S. Corbel, L. Balan, K. Mozet, E. Girot, G. Medjahdi, M. Ben Said, A. Ghrabi, R.
601 Schneider. Porous Mn-doped ZnO nanoparticles for enhanced solar and visible light
602 photocatalysis. Mater. Des. 101 (2016) 309-316.
603 [6] M. Ibn Mahrsi, B. Chouchene, T. Gries, V. Carré, E. Girot, G. Medjahdi, F. Ayari, L. Balan, R.
604 Schneider. Novel ZnO/Ag nanohybrids prepared from Ag^{+}-doped layered zinc hydroxides as
605 highly active photocatalysts for the degradation of dyes and Ciprofloxacin. Colloids Surf. A:
606 Physicochem. Eng. Asp. 671 (2023) 131643.
607 [7] A. Galdámez-Martínez, Y. Bai, G. Santana, R.S. Sprick, A. Dutt. Photocatalytic hydrogen
608 production performance of 1-D ZnO nanostructures: Role of Structural Properties. Int. J.
609 Hydrogen Energy 45 (2020) 31942-31951.
610 [8] X. Wang,, Z. Cao, Y. Zhang, H. Xu, S. Cao, R. Zhang. All-solid-state Z-scheme Pt/ZnS-ZnO
611 heterostructure sheets for photocatalytic simultaneous evolution of H_2 and O_2. Chem. Eng. J.
612 385 (2020) 123782.
613 [9] S. Patial, R. Kumar, P. Raizada, P. Singh, Q. Van Le, E. Lichtfouse, D. Le Tri Nguyen, V.-H.
614 Nguyen. Boosting light-driven CO_2 reduction into solar fuels: Mainstream avenues for
615 engineering ZnO-based photocatalysts. Environ. Res. 197 (2021) 111134.

[10] F.M. Sanakousar, C.C. Vidyasagar, V.M. Jimenez-Perez, K. Prakash. Recent progress on visible-light-driven metal and non-metal doped ZnO nanostructures for photocatalytic degradation of organic pollutants. Mater. Sci. Semicond. 140 (2022) 106390.

[11] S. Goktas, A. Goktas. A comparative study on recent progress in efficient ZnO based nanocomposite and heterojunction photocatalysts: A review. J. Alloys Compd. 863 (2021) 158734.

[12] M. Mrad, B. Chouchene, T. Ben Chaabane, T. Gries, G. Medjahdi, L. Balan, R. Schneider. Heterostructured Photocatalysts Associating ZnO Nanorods and Ag-In-Zn-S Quantum Dots for the Visible Light-Driven Photocatalytic Degradation of the Acid Orange 7 Dye. Catalysts 12 (2022) 1585.

[13] D.S. Murali, S. Kumar, R.J. Choudhary, A.D. Wadikar, M.K. Jain A. Subrahmanyam. Synthesis of Cu2O from CuO thin films: Optical and electrical properties. AIP Adv. 5 (2015) 047143.

[14] M. Haddad, A. Belhadi, L. Boudjellal, M. Trari. Photocatalytic hydrogen production on the heterojunction CuO/ZnO. Int. J. Hydrogen Energy 46 (2021) 37556-37563.

[15] Y.-B. Zhang, J. Yin, L. Li, L.-X. Zhang, L.-J. Bie. Enhanced ethanol gas-sensing properties of flower-like p-CuO/n-ZnO heterojunction nanorods. Sens. Actuators B Chem. 202 (2014) 500-507.

[16] L. Zhu, H. Li, Z. Liu, P. Xia, Y. Xie, D. Xiong. Synthesis of the 0D/3D CuO/ZnO Heterojunction with Enhanced Photocatalytic Activity. J. Phys. Chem. C 122 (2018) 9531-9539.

[17] R.M. Mohamed, A.A. Ismail. Photocatalytic reduction and removal of mercury ions over mesoporous CuO/ZnO S-scheme heterojunction photocatalyst. Ceram. Int. 47 (2021) 9659-9667.

[18] D. Upadhaya, D. Dhar Purkayastha. Self-cleaning activity of CuO/ZnO heterostructure: A synergy of photocatalysis and hydrophilicity. J. Taiwan Inst. Chem. Eng. 132 (2022) 104216.

[19] S. Chabri, A. Dhara, B. Show, D. Adak, A. Sinhab, N. Mukherjee. Mesoporous CuO-ZnO p-n heterojunction based nanocomposites with high specific surface area for enhanced photocatalysis and electrochemical sensing. Catal. Sci. Technol. 6 (2016) 3238-3252.

[20] M.A. Bajiri, A. Hezam, K. Namratha, R. Viswanath, Q.A. Drmosh, H.S. Bhojya Naik, K. Byrappa. CuO/ZnO/g-C_3N_4 heterostructures as efficient visible light-driven photocatalysts. J. Environ. Chem. Eng. 7 (2019) 103412.

[21] A. Dhara, B. Show, A. Baral, S. Chabri, A. Sinha, N. Ratan Bandyopadhyay, N. Mukherjee. Core-shell CuO-ZnO p-n heterojunction with high specific surface area for enhanced photoelectrochemical (PEC) energy conversion. Sol. Energy 136 (2016) 327-332.

[22] S. Pal, S. Maiti, U. Narayan Maiti, K. Kumar Chattopadhyay. Low temperature solution processed ZnO/CuO heterojunction photocatalyst for visible light induced photo-degradation of organic pollutants. CrystEngComm 17 (2015) 1464-1476.

[23] H. Salari, M. Sadeghinia. MOF-templated synthesis of nano Ag_2O/ZnO/CuO heterostructure for photocatalysis. J. Photochem. Photobiol. A: Chem. 376 (2019) 279–287.

[24] H. Yoo, S. Kahng, J.H. Kim. Z-scheme assisted ZnO/Cu_2O-CuO photocatalysts to increase photoactive electrons in hydrogen evolution by water splitting. Sol. Energy Mater. Sol. Cells 204 (2020) 110211.

[25] R. Kumar, K. Kumar, N. Thakur. Biosynthesis of CuO/Cu_2O-ZnO nanocomposites via *Commelina benghalensis* leaf extract and their antibacterial, photocatalytic and antioxidant assessment. Inorg. Chem. Commun. 157 (2023) 111400.

[26] B. Uma, K.S. Anantharaju, L. Renuka, H. Nagabhushana, S. Malini, S.S. More, Y.S. Vidya, S. Meena. Controlled synthesis of (CuO-Cu_2O)Cu/ZnO multi oxide nanocomposites by facile combustion route: A potential photocatalytic, antimicrobial and anticancer activity. Ceram. Int. 47 (2021) 14829-14844.

[27] Y. Lee, E. Kim, Y. Park, J. Kim, W. Ryu, J. Rho, K. Kim. Photodeposited metal-semiconductor nanocomposites and their applications. J. Materiomics 4 (2018) 83-94.

[28] S. Bhardwaj, B. Pal. Photodeposition of Ag and Cu binary co-catalyst onto TiO_2 for improved optical and photocatalytic degradation properties. Adv. Powder Technol. 29 (2018) 2119-2128.

[29] I.A. Mkhalid, A. Shawky. Cu-supported Cu_2O nanoparticles: Optimized photodeposition enhances the visible light photodestruction of atrazine. J. Alloys Compd. 853 (2021) 157040.

[30] M.A. Sliem, T. Hikov, Z.-A. Li, M. Spasova, M. Farle, D.A. Schmidt, M. Havenith-Newen, R.A. Fischer. Interfacial Cu/ZnO contact by selective photodeposition of copper onto the surface of small ZnO nanoparticles in non-aqueous colloidal solution. Phys. Chem. Chem. Phys. 2010, 12, 9858-9866.

[31] J.W.M. Jacobs, F.W.H. Kampers, J.M.G. Rikken, C.W.T. Bulle-l.ieuwma, O.C. Koningsberger. Copper Photodeposition on TiO_2 Studied with HREM and EXAFS. J. Electrochem. Soc. 136 (1989) 2914-2923.

[32] Wang, X.M. Fan, D.Z. Wu, J. Dai, H. Liu, H.R. Liu, Z.W. Zhou. Fabrication of CuO/T-ZnOw nanocomposites using photo-deposition and their photocatalytic property. Appl. Surf. Sci. 258 (2011) 1797-1805.

[33] P.A. Bharad, A.V. Nikam, F. Thomas, C.S. Gopinath. CuO_x-TiO_2 Composites: Electronically Integrated Nanocomposites for Solar Hydrogen Generation. ChemistrySelect 3 (2018) 12022-12030.

[34] S. Rej, M. Bisetto, A. Naldoni, P. Fornasiero. Well-defined Cu_2O photocatalysts for solar fuels and chemicals. J. Mater. Chem. A 9 (2021) 5915-5951.

[35] R. Cuscó, E. Alarcón-Lladó, J. Ibáñez, L. Artús, J. Jiménez, B. Wang, M.J. Callahan. Temperature dependence of Raman scattering in ZnO. Phys. Rev. B 75 (2007) 165202.

[36] Q.K. Doan, M.H. Nguyen, C.D. Sai, V.T. Pham, H.H. Mai, N.H Pham, T.C. Bach, V.T. Nguyen, T.T. Nguyen, K.H. Ho, T.H. Tran. Enhanced optical properties of ZnO nanorods decorated with gold nanoparticles for self cleaning surface enhanced Raman applications. Appl. Surf. Sci. 505 (2020) 144593.

[37] M. Smyrnioti, C. Tampaxis, T. Steriotis, T. Ioannides. Study of CO_2 adsorption on a commercial CuO/ZnO/Al_2O_3 catalyst. Catal. Today 357 (2020) 495-502.

[38] D. Tuncel, A.N. Ökte. ZnO@CuO derived from Cu-BTC for efficient UV-induced photocatalytic applications. Catal. Today 328 (2019) 149-156.

[39] A. Khataee, D. Kalderis, P. Gholami, A. Fazli, M. Moschogiannaki, V. Binas, M. Lykaki, M. Konsolakis. Cu_2O-CuO@biochar composite: Synthesis, characterization and its efficient photocatalytic performance. Appl. Surf. Sci. 498 (2019) 143846.

[40] W. Zhang, X. Chen, X. Zhao, M. Yin, L. Feng, H. Wang. Simultaneous nitrogen doping and Cu_2O oxidization by one-step plasma treatment toward nitrogen-doped Cu_2O@CuO heterostructure: An efficient photocatalyst for H_2O_2 evolution under visible light. Appl. Surf. Sci. 527 (2020) 146908.

[41] M. Deo, S. Mujawar, O. Game, A. Yengantiwar, A. Banpurkar, S. Kulkarni, J. Jog. S. Ogale. Strong photo-response in a flip-chip nanowire p-Cu_2O/n-ZnO junction. Nanoscale 3 (2011) 4706-4712.

[42] Y. Taraka Prabhu, V. Navakoteswara Rao, M. Venkatakrishnan Shankar, B. Sreedhar, U. Pal. The facile hydrothermal synthesis of CuO@ZnO heterojunction nanostructures for enhanced photocatalytic hydrogen evolution. New J. Chem. 2019, 43, 6794-6805.

[43] B. Panigrahy, M. Aslam, D.S. Misra, M. Ghosh, D. Bahadur. Defect-Related Emissions and Magnetization Properties of ZnO Nanorods. Adv. Funct. Mater. 20 (2010) 1161-1165.

[44] S. Mukhopadhyay, P. Pratim Das, S. Maity, P. Ghosh, P. Sujatha Devi. Solution grown ZnO rods: Synthesis, characterization and defect mediated photocatalytic activity. Appl. Catal. B: Environ. 165 (2015) 128-138.

[45] M. Parolini. Toxicity of the Non-Steroidal Anti-Inflammatory Drugs (NSAIDs) acetylsalicylic acid, paracetamol, diclofenac, ibuprofen and naproxen towards freshwater invertebrates: A review. Sci. Total Environ. 740 (2020) 140043.

[46] D. Wojcieszyńska, U. Guzik. Naproxen in the environment: its occurrence, toxicity to nontarget organisms and biodegradation. Appl. Microbiol. Biotechnol. 104 (2020) 1849-1857.

[47] A. Romeiro, M.E. Azenha, M. Canle, V.H.N. Rodrigues, J.P. Da Silva, H.D. Burrows. Titanium Dioxide Nanoparticle Photocatalysed Degradation of Ibuprofen and Naproxen in Water: Competing Hydroxyl Radical Attack and Oxidative Decarboxylation by Semiconductor Holes. ChemistrySelect 3 (2018) 10915-10924.

[48] M. Kohantorabi, G. Moussavi, S. Mohammadi, P. Oulego, S. Giannakis. Photocatalytic activation of peroxymonosulfate (PMS) by novel mesoporous Ag/ZnO@$NiFe_2O_4$ nanorods, inducing radical-mediated acetaminophen degradation under UVA irradiation. Chemosphere 277 (2021) 130271.

[49] F.F.A. Aziz, A.A. Jalil, N.S. Hassan, A.A. Fauzi, M.S. Azami, N.W.C. Jusoh, R. Jusoh. A review on synergistic coexisting pollutants for efficient photocatalytic reaction in wastewater remediation. Environ. Res. 209 (2022) 112748.

[50] N. Jallouli, K. Elghniji, O. Hentati, A.R. Ribeiro, A.M.T. Silva, M. Ksibi. UV and solar photo-degradation of naproxen: TiO_2 catalyst effect, reaction kinetics, products identification and toxicity assessment. J. Hazard. Mater. 304 (2016) 329-336.

[51] M. Jimenez-Salcedo, M. Monge, M.T. Tena. The photocatalytic degradation of naproxen with g-C_3N_4 and visible light: Identification of primary by-products and mechanism in tap water and ultrapure water. J. Environ. Chem. Eng. 10 (2022) 106964.

[52] P.J. Mafa, M.E. Malefane, A.O. Idris, D. Liu, J. Gui, B.B. Mamba, A.T. Kuvarega. Multi-elemental doped g-C_3N_4 with enhanced visible light photocatalytic activity: Insight into naproxen degradation, kinetics, effect of electrolytes, and mechanism. Sep. Purif. Technol. 282 (2022) 120089.

743 [53] Y. Xu, M. A. A. Schoonen, The absolute energy positions of conduction and valence
744 bands of selected semiconducting minerals, Am. Mineral. 85 (2000) 543-556.
745